ACS Combinatorial Science

Research Article

pubs.acs.org/acscombsci

Structure–Property–Composition Relationships in Doped Zinc Oxides: Enhanced Photocatalytic Activity with Rare Earth Dopants

Josephine B. M. Goodall,[†,§] Derek Illsley,[‡] Robert Lines,[‡] Neel M. Makwana,[†] and Jawwad A. Darr*,[†]

[†]Christopher Ingold Laboratories, Department of Chemistry, University College London, 20 Gordon Street, London WC1H 0AJ, United Kingdom

[‡]Sun Chemical, St Mary Cray, Kent BR5 3PP, United Kingdom

Supporting Information

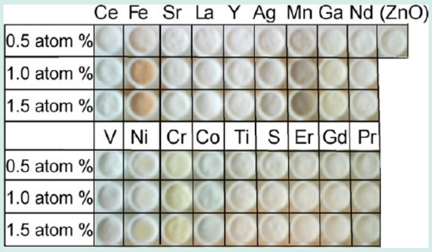

ABSTRACT: In this paper, we demonstrate the use of continuous hydrothermal flow synthesis (CHFS) technology to rapidly produce a library of 56 crystalline (doped) zinc oxide nanopowders and two undoped samples, each with different particle properties. Each sample was produced in series from the mixing of an aqueous stream of basic zinc nitrate (and dopant ion or modifier) solution with a flow of superheated water (at 450 °C and 24.1 MPa), whereupon a crystalline nanoparticle slurry was rapidly formed. Each composition was collected in series, cleaned, freeze-dried, and then characterized using analytical methods, including powder X-ray diffraction, transmission electron microscopy, Brunauer–Emmett–Teller surface area measurement, X-ray photoelectron spectroscopy, and UV–vis spectrophotometry. Photocatalytic activity of the samples toward the decolorization of methylene blue dye was assessed, and the results revealed that transition metal dopants tended to reduce the photoactivity while rare earth ions, in general, increased the photocatalytic activity. In general, low dopant concentrations were more beneficial to having greater photodecolorization in all cases.

KEYWORDS: *continuous hydrothermal, zinc oxide, photocatalytic activity, doping, UV attenuator*

INTRODUCTION

Zinc oxide is a white wide-band-gap semiconductor that is widely used as an additive in numerous materials and products. It is used in optoelectronic devices,[1] in the rubber industry to increase the cure rate, and as a fungicide to retard the growth of mold.[2,3] Zinc oxide imparts a unique combination of properties in glasses: it reduces the coefficient of thermal expansion and the specific heat, increases the conductivity, imparts high brilliance and luster, and confers high stability against deformation under stress.[4,5] Zinc oxide is also used in many cosmetic applications, especially sunscreens.[6] Zinc oxide can be used as a gas sensor material; bulk and thin-film zinc oxide also shows a high sensitivity to toxic gases. Zinc oxide is also used in electrical devices such as acoustic resonators because it has a strong piezoelectric effect.[7]

Nano-ZnO has been synthesized by many methods in the literature, including reactions in non-aqueous media (e.g., ethanol-based systems) and complex multistep syntheses. Music et al.[8] reported the synthesis of ca. 100 nm zinc oxide particles by refluxing of the precursors at 90 °C in water for 24 h, followed by heat treatment at 600 °C for 8 h in air. Wang et al.[9] synthesized zinc oxide nanoparticles (size range 50 to 200 nm) using a batch solvothermal method at 180 °C for 24 h. More well-known ZnO synthesis techniques include metal-organic chemical vapor deposition, spray pyrolysis, electrochemical synthesis, laser ablation, sputter deposition, and vapor transport.[10−15] Complex morphologies can be achieved for nanoparticles of ZnO because of preferential growth directions as a result of intrinsic high-energy facets.[16]

Continuous hydrothermal flow synthesis (CHFS) routes offer a potential rapid method of producing ZnO crystalline nanoparticles from simple precursors in an aqueous system.[17−20] In CHFS, a feed of superheated water is mixed with a metal-salt-containing feed (often in the presence of base), which results in rapid hydrolysis and dehydration of the metal salt to form metal oxide nanoparticles (<100 nm in diameter). ZnO made via continuous hydrothermal methods has been investigated in detail by a number of groups worldwide, including Arai and co-workers,[17−20] and Viswanathan and co-workers.[21,22] Because of the continuous nature of CHFS, it also offers a method to produce libraries of compositionally unique doped ZnO materials by sequentially feeding a series of different Zn-containing precursor materials into the reactor and harvesting the slurries in series.[23] This approach is very effective because it allows a large number of samples to be made in a short period of time.

Doping of elements into semiconductors is used to introduce energy states in the band gap and reduce carrier recombination as well as to extend the band gap into the visible spectrum.[24] There is much literature on the doping of titania, where dopants can act as trapping sites for electrons or holes to

Received: July 11, 2014
Revised: December 1, 2014
Published: January 2, 2015

DOI: 10.1021/co500109f
ACS Comb. Sci. 2015, 17, 100−112

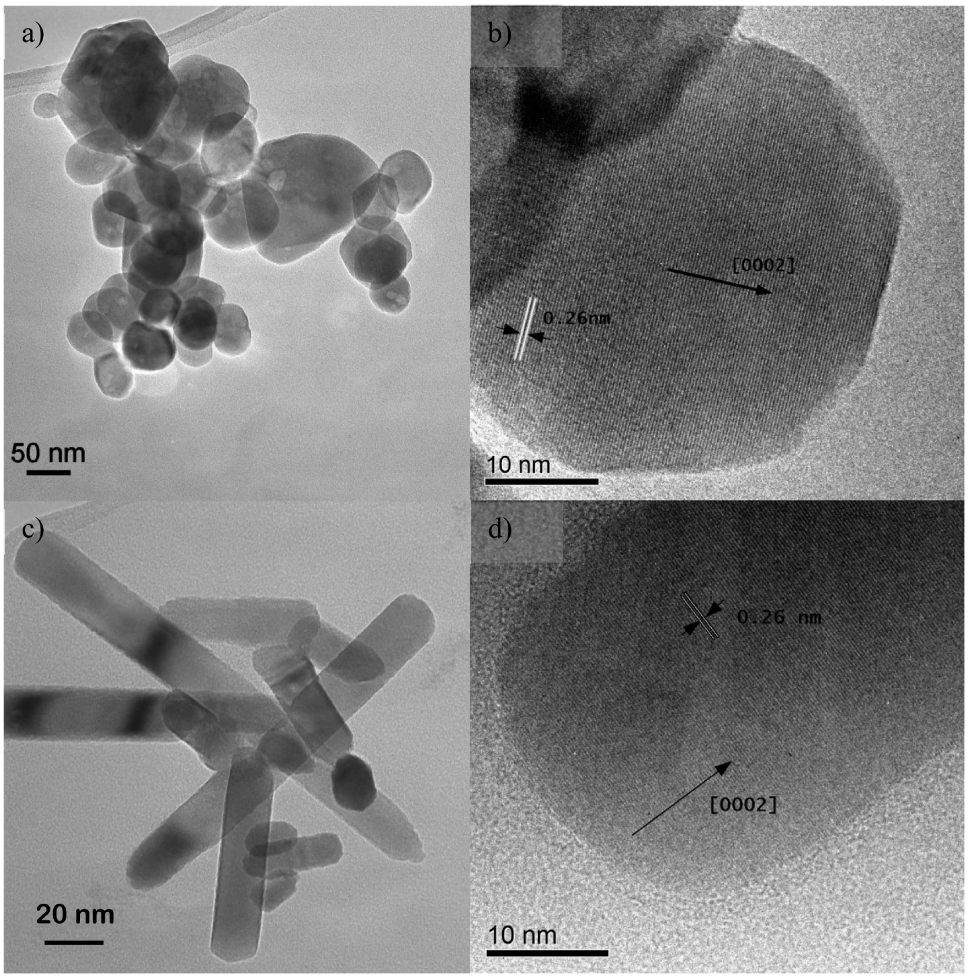

Figure 1. TEM images of (a) ZnO-a and (c) ZnO-b and HRTEM images of (b) ZnO-a and (d) ZnO-b showing the (0002) interplanar spacing and [0002] direction.

promote charge separation[25] or can act as defects to enhance recombination.[26] There has been comparatively much less research into the doping of zinc oxide for photocatalyst materials or UV attenuators, and the measured properties vary according to factors such as the synthesis method and substrate. By using CHFS and various dopants in ZnO that have been shown in the literature to affect the optical properties in ZnO or TiO_2, it is possible to rapidly create a library of doped nanomaterials to investigate the effects of doping of ZnO on photocatalytic activity.

Rare earth dopants such as lanthanum have been reported to increase the photocatalytic activity of ZnO for the degradation of organics such as 2,4,6-trichlorophenol, when added in small amounts (ca. 1 atom %).[27] Transition metal dopants have a varied effect on the optical and photocatalytic properties of ZnO. Silver doping in ZnO reportedly increases the activity toward a range of substrates, including methylene blue and phenol,[28] while cobalt and manganese doping reportedly decreases the photoactivity.[29,30] However, in other reports, manganese, cobalt, and nickel ions (1 atom %) and iron dopants were all found to increase the photoresponse of ZnO.[31,32] In this paper, we report the use of CHFS to rapidly produce a library of compositionally unique crystalline doped zinc oxide nanopowders. This allowed a comparison of a wide range of dopants used to modify the properties of ZnO to produce differing UV-attenuating and photocatalyst materials. Very different photocatalytic activities were measured, and the particle properties were highly sensitive to the different dopants used.

RESULTS AND DISCUSSION

Nanozinc oxide was obtained as a fine white powder. The doped ZnO materials were white or pale-colored. Ca-, Cr-, and Ce-doped ZnO were yellow, and Fe-doped ZnO was orange. Silver and manganese doping caused a brown color, and Co-doped ZnO was blue. In all cases, the intensity of the color increased with doping level (L*a*b* color coordinates are shown in Tables S3 and S4 in the Supporting Information). ZnO powders are often used in UV-attenuation applications where intense color may not be beneficial for aesthetic reasons. In photocatalytic applications, color may indicate visible absorption, extending the photoresponse, but it may also indicate color centers, which can act as sites for recombination.

A transmission electron microscopy (TEM) image of ZnO-a is shown in Figure 1a; the average particle size is 53.1 ± 22 nm (based on 215 particles), and the particles were polygonal in shape. The high-resolution TEM (HRTEM) image of ZnO-a in Figure 1b shows lattice fringes that are coherent across a single particle. The average lattice spacing was calculated as 0.26 nm, which is consistent with the ZnO(0002) interplanar spacing.[33] The TEM image of ZnO-b (made with added hydrogen peroxide) (Figure 1c) shows ZnO rods with dimensions of

DOI: 10.1021/co500109f
ACS Comb. Sci. 2015, 17, 100−112

approximately 60 nm × 15 nm (59.5 ± 24.5 nm × 15.4 ± 4.8 nm based on 220 particles). The HRTEM image (Figure 1d) shows the end of a ZnO-b rod with the characteristic (0002) lattice spacing of 0.26 nm (mean). The (0002) plane is marked. These facets are polar because of the position of Zn^{2+} and O^{2-} ions in the lattice and have a higher surface energy than other ZnO facets.[16] H_2O_2 decomposition in the reactor most likely aids in the formation of soluble peroxo species, which allows growth in the fast growth directions such as ±[0001]. It has been suggested in the literature that the [0001] direction grows through the addition of soluble ZnO_2^{2-} growth units onto the Zn^+ that forms the (0001) planes and surface O^{2-} on the $(000\bar{1})$ planes.[34] In alkali solutions, the growth faces are shielded by OH^- ligands, which reduce the growth velocity in directions including the [0001] direction.[35] This suggests that the presence of H_2O_2 in the feed disrupts the OH^- ligands at the surface of nuclei.

All of the powders showed X-ray diffraction (XRD) patterns consistent with a wurtzite structure (Figure S1 in the Supporting Information). This is in keeping with the literature, where dopants have been found to readily substitute into the zinc lattice. The solubility of cerium dioxide in ZnO has been reported to be as low as 2 atom % Ce,[36] while Jakani et al.[32] suggested that the solubility of nickel in ZnO is limited to ca. 1 atom %. However, in other reports, nickel has been doped up to ca. 12 atom %.[37] Dopant levels of up to 5 atom % for transition metal dopants such as manganese and cobalt and 10 atom % for iron have been reported elsewhere, with no sign of phase separation in the doped ZnO XRD patterns.[29,30] Many of these differences are due to the different synthesis conditions used.

The specific surface area of materials affects the adsorption of substrate molecules and the number of sites for photocatalytic reactions. Other factors influencing the photocatalytic activity include the structure and crystallinity, and the defect concentration and type also need to be considered. The Brunauer−Emmett−Teller (BET) surface area of undoped zinc oxide (ZnO-a) was 33.4 ± 1.0 $m^2\ g^{-1}$, and that of ZnO made with H_2O_2 (ZnO-b) was 41.6 ± 1.0 $m^2\ g^{-1}$. All of the doped samples possessed BET surface areas in the range 23.8 to 45.3 $m^2\ g^{-1}$. The BET surface area results and comparisons of crystallite sizes calculated from the Scherrer equation (using the $(10\bar{1}1)$ reflection) are shown in Figure 2. Generally the specific surface area increased as the calculated crystallite size decreased, suggesting that changes in surface area are related to a change in size rather than to porosity or agglomeration. Sulfur-, titanium-, iron-, and vanadium-doped samples had higher surface areas than the undoped zinc oxide, which may be due to decreased size or reduced agglomeration. The rare earth dopants tended to reduce the surface area of the ZnO powders, which could be a result of increasing particle size.

It is well-documented for zinc oxide that different facets have different energies, e.g., the [0001] and the $[10\bar{1}0]$ directions are fast-growth directions as a result of the need to stabilize these high-energy facets.[16] Figure 3 shows the ratios of the intensities of the (0002) and the $(10\bar{1}0)$ diffraction peaks calculated from the XRD data. It has been noted for ZnO that morphology and texture can have a significant effect on the Bragg intensities.[38,39] In undoped zinc oxide, the ratio is close to 1:1, and when compared to the TEM images (Figure 1a,b), this suggests that the two directions grew approximately equally. In the case of the ZnO-b sample, the ratio was ca. 0.82, which correlates well with the rodlike particles seen by TEM (Figure 1c,d). It can be seen that rare earth dopants, sulfur, gallium, and cobalt produced $(0002)/(10\bar{1}0)$ peak intensity ratios of ca. 0.7. This could suggest that the (0002) plane is suppressed relative to the $(10\bar{1}0)$ plane or, less likely, could be due to texture or preferential alignment in the flat-plate XRD. It has been reported elsewhere that sulfur-doped zinc oxide nanostructures (made by annealing ZnS in oxygen) and gallium-doped zinc oxide films form polycrystalline zinc oxide rather than columnar structures.[40,41] Sulfur doping was found to reduce the relative intensity of the (0002) peak when the material was synthesized by the sol−gel process.[42] However, S-doped ZnO nanorods (with increased relative (0002) intensity) can be synthesized by batch hydrothermal methods at low temperatures.[43] Herein, transition metal and strontium dopants tended to have little effect on the $(0002)/(10\bar{1}0)$ peak intensity ratio compared to that of ZnO-a, giving a value of ca. 0.9, suggesting that these particles may have a more isotropic shape similar to that of

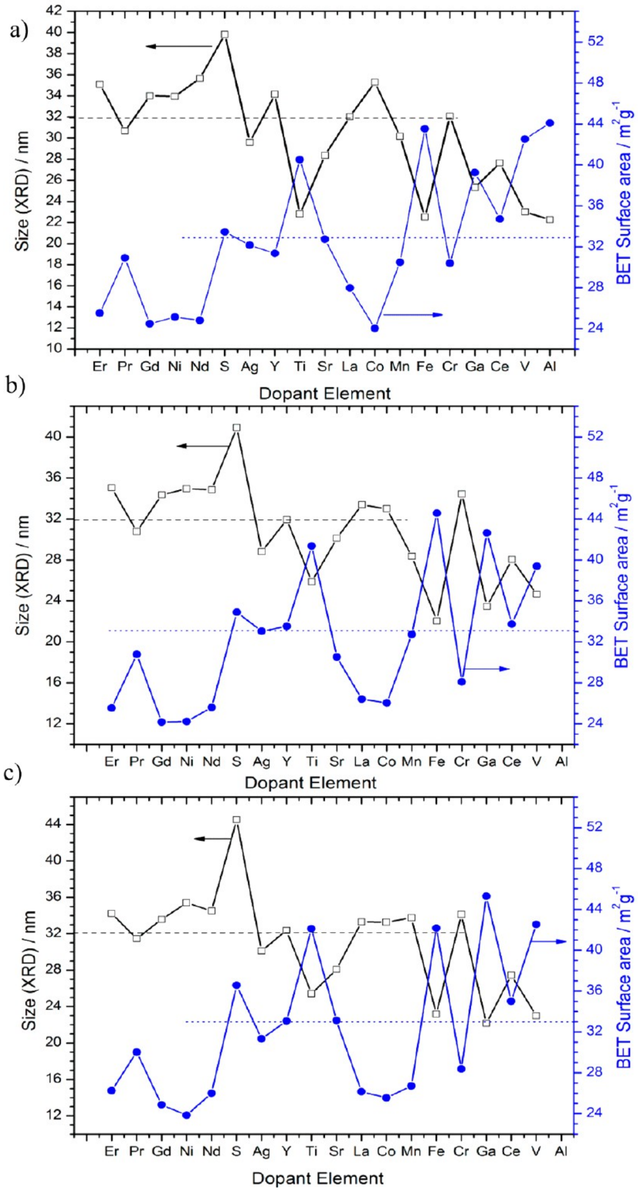

Figure 2. Variation in size (black □) and BET surface area (blue ●) for (a) 0.5 atom %, (b) 2.5 atom %, and (c) 5.0 atom % doping levels. Dotted lines represent values for undoped ZnO (ZnO-a).

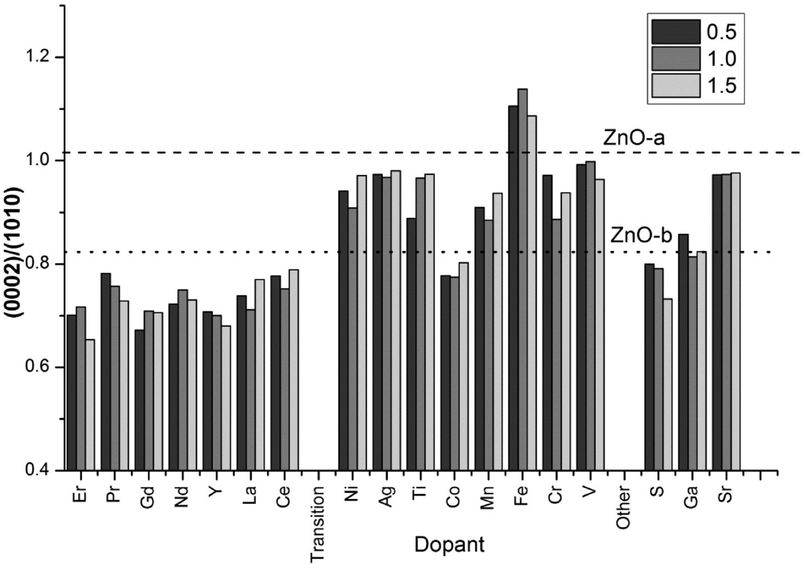

Figure 3. Ratios of the intensities of the (0002) and (10$\bar{1}$0) XRD peaks.

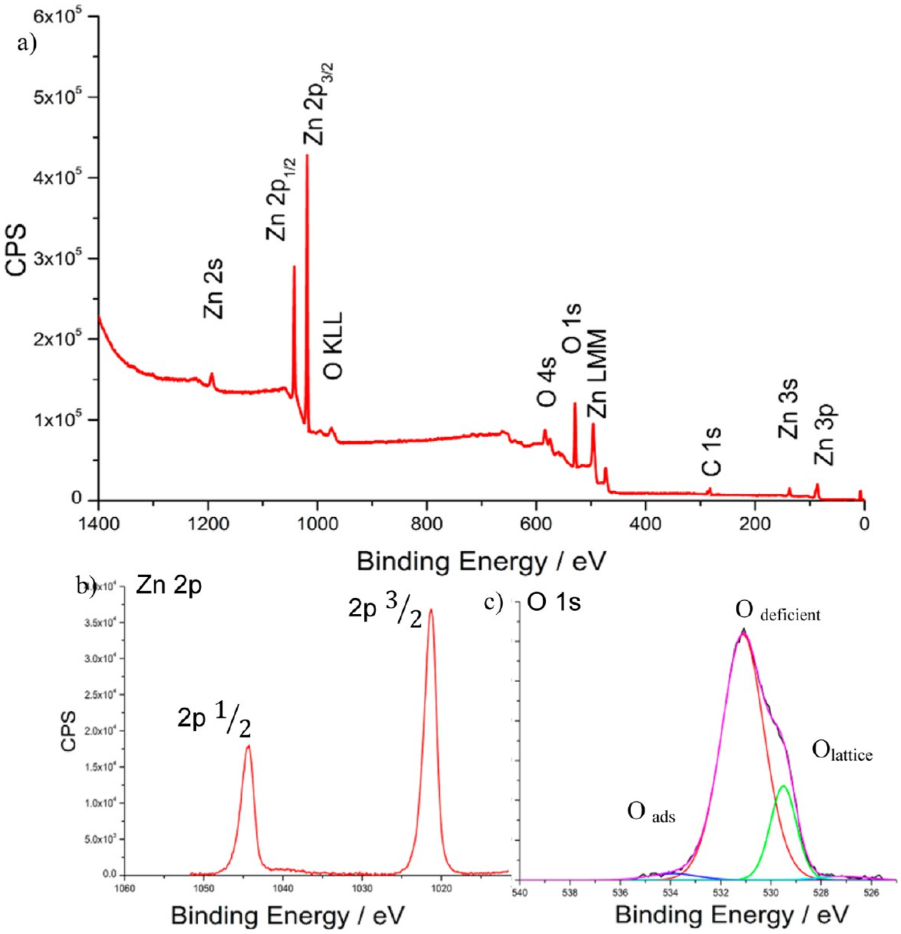

Figure 4. (a) XPS survey spectrum and spectra of the (b) Zn 2p and (c) O 1s regions for undoped ZnO.

undoped ZnO. This is similar to results found in the literature, where doping of zinc oxide with nickel, manganese, chromium, cobalt, vanadium, and iron at 1 atom % (via sol–gel synthesis processes) was reported to have little effect on the morphology compared with undoped zinc oxide.[44]

X-ray photoelectron spectroscopy (XPS) was used to examine all of the 1.5 atom % doped samples; in addition to the survey spectra, with two main spectral regions, Zn 2p and O 1s, detailed spectra of the dopant environment were recorded. Figure 4 shows the survey spectrum and high-resolution spectra of the Zn 2p and O 1s regions of undoped zinc oxide. It has a

Zn $2p^{3/2}$ binding energy (BE) of 1021.92 eV with a spin−orbit coupling of 23 eV (Figure 4b). The O 1s peak for the ZnO samples was found at 530.9 eV and was resolved into three peaks; a low-energy peak at 529.5 eV, an intermediate-energy peak at 530.1 eV, and a small high-energy peak at 533.6 eV (Figure 4c). This is consistent with values in the literature for ZnO nanoparticles and thin films.[37,45−47] The low-energy peak is attributed to O^{2-} in the wurtzite lattice ($O_{lattice}$). The intermediate-energy peak (at ca. 530 eV) is attributed to O^{2-}-deficient areas of the wurtzite lattice such as the surface ($O_{deficient}$), and the high-energy peak is due to chemisorbed surface species such as hydroxyl groups, loosely bound oxygen, or water (O_{ads}).[37,46] The peak due to oxygen deficiencies has been reported to be higher than the lattice peak at the surface of ZnO films.[47]

Table 1 shows the dopant concentration at the ZnO surface, the oxidation state, and the characteristic dopant binding energy for each of the nominally 1.5 atom % doped samples (selected high-resolution envelopes are shown in Figures S2−S4 in the Supporting Information). The atom percentages calculated for the dopants suggest that most of the dopants were preferentially located at or near the surface, as the percentage of dopant in the XPS analysis of the survey scans was generally greater than 1.5%. In contrast, 1.5S had only 1.0% sulfur, suggesting that either the sulfur was in the bulk or the incorporation of S into zinc oxide was limited. The exact oxidation state of manganese could not be defined from the XPS spectra. All of the dopant spectra displayed peaks at their expected energies, suggesting that all of the dopants were incorporated nanoparticles. In addition, no peaks due to metallic elements were found, suggesting that the dopants were indeed incorporated either into or as defects in the zinc oxide lattice.

Table 1. XPS Results for Dopant Ions in 1.5 Atom % Doped ZnO Samples

sample	dopant atom %[a]	dopant oxidation state	dopant binding energy/eV
1.5V	2.8	5+, 4+ (3+/2+)	517.3, 516.7, 513.5
1.5Pr	1.2	3+	933.4
1.5Nd	3.1	3+	979.3
1.5Gd	2.0	3+	1187.1
1.5Er	3.1	3+	169.9
1.5La	2.3	3+	835.8
1.5Y	2.5	3+	158.0
1.5Fe	3.0	3+	710.8
1.5Ti	3.3	4+	1021.9
1.5Co	2.0	2+	779.6
1.5Cr	2.6	3+	577.4
1.5Sr	1.3	2+	133.2
1.5Ni	1.4	2+	855.5
1.5Ag	2.0	1+	366.5
1.5Ga	1.9	3+	1118.2
1.5Ce	2.5	3+, 4+	884.5
1.5S	1.0	−1	166.8
1.5Mn	2.1	~	641.7

[a] The dopant content was calculated with respect to the total metal ion content only: dopant content = $M^{n+}/(Zn^{2+} + M^{n+})$.

Figure 5 shows the UV−vis absorption spectra for the 1.5 atom % transition-metal-doped samples. All of the samples exhibited a sharp transition at ca. 400 nm between UV absorption and the visible region, as would be expected for the zinc oxide host lattice. In addition, manganese doping caused increased absorption over the entire visible range, which is attributed to d−d electron transitions over the entire visible range.[32] Silver-doped zinc oxide also displayed increased absorbance between ca. 400 and 800 nm due to d−d transitions. This is consistent with the color shift from white to brown. The vanadium-doped sample had three minor transitions at ca. 480, 560, and 850 nm that were assigned to d−d transitions in the V^{2+} oxidation state.[44,48] This assignment agrees with the corresponding XPS spectra, where a characteristic energy peak due to a low valence state was seen at ca. 513 eV.

The 1.5Co sample had increased absorption in the UV−vis spectrum between ca. 570 and 700 nm due to $^4A_2$−$^4T_1$ transitions and strong spin coupling. This band split into three transitions that are seen at 570, 610 and 660 nm, assigned in the literature to transitions from the $^4A_2$ ground state to the $^4T_1(P)$, $^2A_1(G)$, and $^2E(G)$ levels, respectively.[29,32] Similar bands were also seen in the Ni^{2+}-doped sample and were assigned to $^3T_1(F)$−$^3T_1(P)$ transitions.[31] Additionally, in the 1.5Ni sample, the transition between UV-absorbing and visible wavelengths had a tail in the range from ca. 400 to 450 nm, accounting for the yellow color. Chromium-doped zinc oxide had increased absorbance between 400 and 540 nm.[44] The 1.5Fe sample had increased absorbance between 400 and 550 nm with two separate bands at ca. 450 and 510 nm, accounting for the yellow−orange color. These absorption bands are attributed to Fe^{3+} in tetrahedral and octahedral states.[44]

The band gap of the transition-metal-doped zinc oxide edge had a slight to negligible red shift (lower energy) in all cases (0.01−0.04 eV). This red shift has been reported to be due to d−d transitions and exchange interactions between the band electrons and localized dopant electrons.[29,37] The red shift was greatest for Cr- and Co-doped ZnO. The band gap of the 1.5Cr sample was calculated as 2.25 eV, which can be compared to those of ZnO-a at 3.30 eV and ZnO-b at 2.29 eV.

Figure 6 shows the rate constant (pseudo-first-order) for the photocatalytic decolorization of methylene blue (MB). It is well-known that MB can be degraded via a direct or indirect mechanism. In the indirect mechanism, upon photoexcitation of a semiconductor and subsequent photogeneration of charge carriers ($e^- + h^+$), a number of photocatalytic processes can occur, leading to the formation of reactive oxygen species (ROS) such as hydroxyl radical ($OH^\bullet$), hydroperoxyl radical ($HO_2^\bullet$), and superoxide radical ($O_2^{\bullet-}$). These radicals are highly reactive intermediates that will attack the dye molecules, eventually leading to complete mineralization of the dye. Dye molecules can also be directly reduced or oxidized by electrons or holes, respectively. In the direct mechanism, known as the dye-sensitized mechanism, under visible-light irradiation ($\lambda >$ 400 nm) the dye can be photosensitized to an excited state (MB*), which then injects an electron into the conduction band of the semiconductor, forming a cationic dye radical ($MB^{\bullet+}$). The electron can participate in photocatalytic processes leading to the formation of ROS, which can attack the unstable cationic dye radicals, leading to mineralization of the dye.[49,50] In this mechanism, the MB may act as a photosensitizer, which can alter the overall degradation reaction. However, in the work presented herein, the degradation of MB appeared to follow first-order kinetics, similar to that observed by Thompson et al.[51] It is also known that MB can self-degrade in the absence of a photocatalyst, and

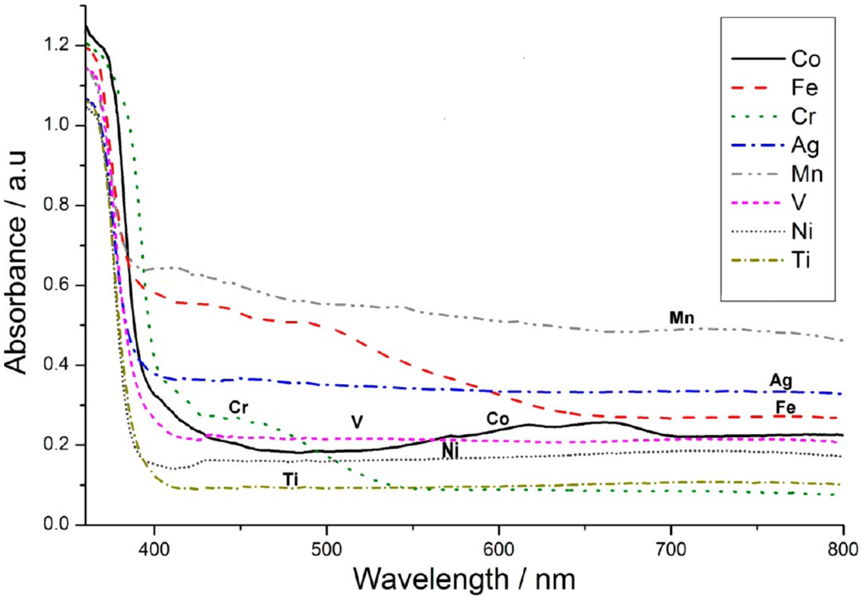

Figure 5. UV−vis spectra of samples doped with transition metals at nominally 1.5 atom %.

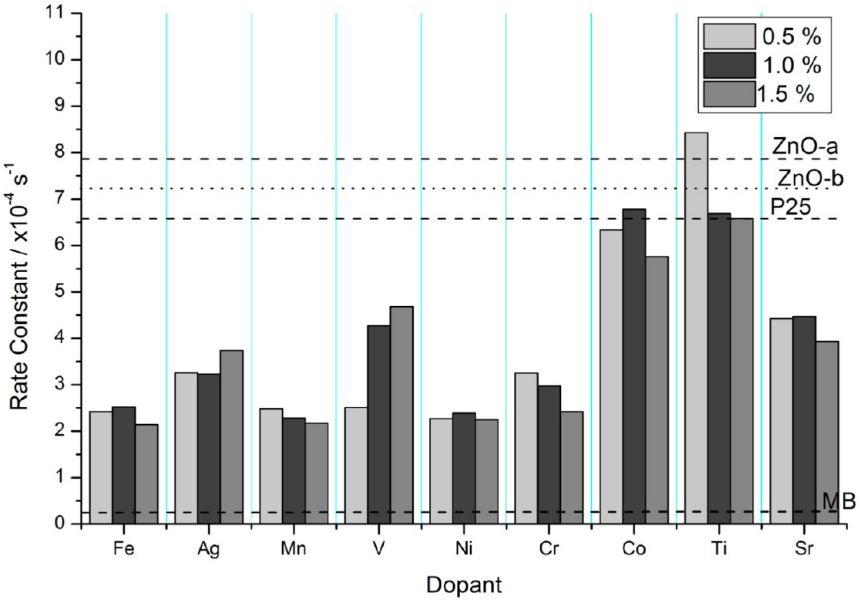

Figure 6. First-order rate constants for the decolorization of methylene blue (MB) by zinc oxide doped with transition metals. Values for undoped ZnO, Aeroxide P25 TiO_2, and the degradation of self-sensitized MB are indicated with dotted lines.

taking this into account, we conducted studies to determine how the rate constant for degradation varies with the concentration of the dye (in the absence of a photocatalyst; data not shown). At the dye concentration used throughout this work (4.0×10^{-5} M), the self-degradation rate of MB is less than 4×10^{-5} s^{-1} (shown in Figure 6). Therefore, this method of photocatalytic testing is wholly appropriate for screening the large sample library prepared in this work.

In general, it appeared that transition metal dopants suppressed the photocatalytic activity of ZnO. Titanium at 0.5 mol % (sample 0.5Ti) was the only transition metal dopant in this library that increased the activity above that of the undoped level. This suggests that at low doping levels Ti^{4+} ions in ZnO favor charge separation. The photocatalytic activity of Ti-doped ZnO decreased with increasing dopant level, presumably because of increasing recombination at defects in the lattice. Mn^{2+} and Co^{2+} doping have been reported to create energy levels deep in the band gap that can act as efficient centers for recombination.[30] Mn, Co, Ni, and Fe doping have all been found to be efficient in reducing and controlling the photoactivity of ZnO for UV-filter applications.[52] In visible-light-only tests, both manganese doping and cobalt doping have been reported to give a higher photocatalytic activity than for undoped ZnO.[53,54] However, in UV-light-only tests, doping with such ions reportedly suppresses the photoactivity.[29] This is likely to be due to the increased visible absorption of doped zinc oxide. Our photodecolorization test method used a mixed UV and visible source, and an increase in activity compared with undoped ZnO was not seen. In addition, in the 1.5Mn sample it was likely that mixed oxidation states existed. Mn had a very low activity at all three doping levels, and the activity decreased with increasing doping, suggesting that Mn ions act

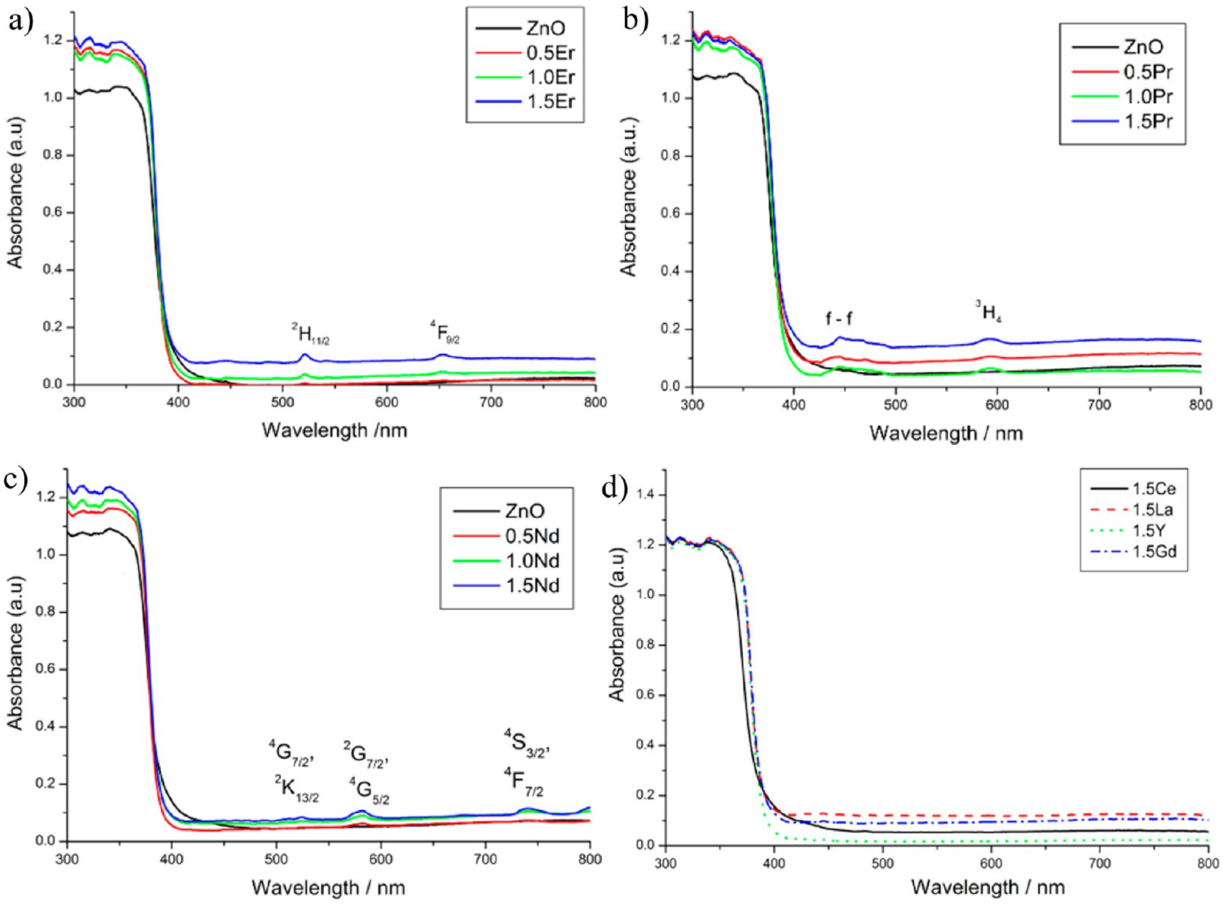

Figure 7. UV−vis spectra of (a) Er-doped samples, (b) Pr-doped samples, (c) Nd-doped samples, and (d) samples doped with other rare earths at 1.5 atom %.

as efficient recombination centers (despite the increased absorbance due to the presence of Mn ions).[31]

It has been calculated that when Cr is doped into ZnO, the Fermi level shifts toward the conduction band and ZnO becomes n-doped.[55] In addition, there is increased absorption in the visible region (as observed herein). Chromium ions are thought to locate at the energetically favorable octahedral sites, whereas Mn and Fe ions are thought to locate at tetrahedral sites and create midband energy levels (ca. 1 eV above the valence band).[32]

It was observed that Co^{2+} doping gave photoactivity comparable to that of Aeroxide TiO_2 P25, and the 1.0Co sample had the highest activity of the three dopant levels. The trend is normally associated with a balance between increased charge separation and the dopant acting as a recombination defect. As the activity of the samples was suppressed compared with the undoped level, this suggests that there is a balance between the Co^{2+} ion deep levels acting as recombination centers and the increased absorption in the visible region (due to Co^{2+} excited levels). Vanadium doping was shown to reduce the photocatalytic activity at all levels; the photoactivity increased slightly with increasing doping content but was still less than that of the undoped sample. Iketani et al.[56] reported that in titania, the existence of V^{4+} promoted photocatalytic activity, whereas V^{5+} appeared to suppress photocatalytic activity. Choi et al.[24] reported that in titania, the V^{5+} energy level is above the valence band and can only act as an electron trap, whereas V^{4+} can trap both electrons and holes, preventing charge recombination. Both V^{4+} and V^{5+} existed in the 1.5V sample, and thus, it could be that V^{5+} was present in the 0.5V sample and that as the concentration of dopant increased, some was reduced to V^{4+} (and lower valence states) to stabilize the structure. The presence of V^{4+} could account for the increased photocatalytic activity compared with the 0.5V sample. Further investigation of the mechanism of vanadium doping in zinc oxide and the valence state of vanadium in zinc is needed.

Strontium-doped ZnO had reduced activity at all three dopant levels. In magnesium-doped ZnO, the photocatalytic activity was increased because of the presence of Mg 3s energy levels located below the ZnO conduction band, which enhanced the reduction potential of the catalyst by shifting the effective level of the conduction band closer to the Fermi level. However, above ca. 5 atom %, the photocatalytic activity was reduced as a result of the presence of magnesium ions as interstitial defects, causing recombination.[57] Because Sr^{2+} ions are larger than Mg^{2+} ions, they may not substitute as readily into the lattice and thus may form interstitial defects, enhancing recombination and suppressing the activity.

The UV−vis absorption spectra of Er-, Pr-, and Nd-doped samples showed characteristic transitions (Figure 7). The UV−vis spectra for the Er-doped samples (Figure 7a) revealed two additional absorptions ca. 521 and 651 nm attributed to transitions from the $^4I_{15/2}$ ground state to the $^2H_{11/2}$ and $^4F_{9/2}$ excited states, respectively.[58] These are similar to the transitions seen in Er-doped TiO_2. Similarly, the Pr-doped ZnO samples (Figure 7b) had additional absorptions at 446 nm (2.79 eV) and 592 nm (2.10 eV) that were assigned to f−f and $^1D_2$−$^3H_4$ transitions, respectively.[59] The spectra of the Nd-doped

DOI: 10.1021/co500109f
ACS Comb. Sci. 2015, 17, 100−112

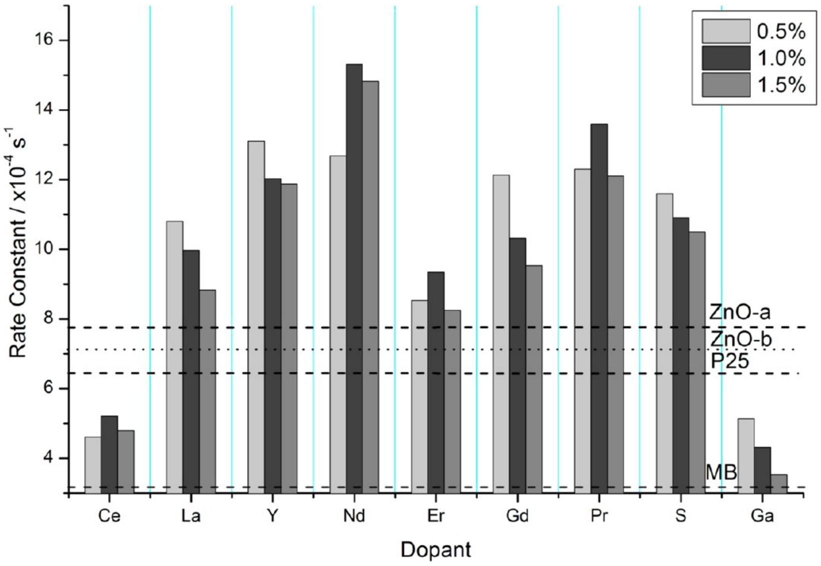

Figure 8. First-order rate constants for the decolorization of methylene blue for zinc oxide doped with rare earth metals. Values for undoped ZnO, Aeroxide P25 TiO_2, and the degradation of self-sensitized MB are indicated with dotted lines.

samples displayed three characteristic bands at 525 nm (2.36 eV), 581 nm (2.14 eV), and 744 nm (1.67 eV), assigned to $^4I_{9/2} \rightarrow {}^2K_{13/2}$ and $^4G_{7/2}$, $^4I_{9/2} \rightarrow {}^2G_{7/2}$ and $^4G_{5/2}$, and $^4I_{9/2} \rightarrow {}^4S_{3/2}$ and $^4F_{7/2}$ transitions, respectively (Figure 7c).[60] In addition Nd, Pr, and Er doping increased the UV absorption relative to that of the undoped ZnO. There is a slight tail in the 1.5Ce spectrum that accounts for the yellow color. Other dopants did not significantly affect the UV−vis spectra of ZnO. A very slight red shift due to transitions between the dopant and the band gap of ZnO was present in almost all cases of rare earth doping (Table S2 in the Supporting Information). The shift in the band gap was less than 0.02 eV in all cases, which is consistent with the low doping levels and color of the rare-earth-doped zinc oxides.

Figure 8 shows the pseudo-first-order rate constants for the decolorization of MB dye. In general, doping of ZnO with rare earth metals increased the photocatalytic activity. The exception is Ce doping, where the photocatalytic activity is suppressed. In all almost cases, for 1.5 atom % doping, the activity was suppressed compared with the less-doped samples (0.5 or 1.0 atom %). For La, Y, and Gd doping, the photocatalytic activity of the nominally 1.0 atom % doped sample was less than that of the 0.5 atom % doped sample. It has been found in the literature that for La doping, the surface energy barrier is effectively increased and the space-charge region narrows, which promotes effective charge separation.[61] Reportedly, above 0.8 wt %, La distorts the ZnO lattice and acts as a defect. Additionally, as the dopant concentration increases, the penetration depth (of light) can exceed the space-charge region, resulting in recombination as the electrons and holes are not separated.[27] Ce ion doping obviously has a different effect on the photocatalytic activity of ZnO compared with other lanthanide dopants. It has been found to suppress the activity for the degradation of aldehydes,[36] and mixed CeO_2−ZnO oxides with 10 atom % Ce, suppressed photocatalytic activity compared with that of ZnO (though CeO_2 was present as well as ZnO).[62] It has also been reported that the presence of Ce ion clusters in the structure reduces the conductivity of ZnO,[63] and the presence of CeO_2 on the ZnO surface suppressed the activity.[36] Sin et al.[64] studied M-doped ZnO compounds (where M = Nd, Eu, or Ce), and found that Nd-doped ZnO had the highest photoactivity and Ce-doped ZnO the lowest; the present work reports similar findings. The improved photocatalytic activity for the rare-earth-doped samples is attributed to efficient electron trapping followed by electron transfer. The dopant ion is reduced upon trapping an electron, which is then followed by the transfer of the electron to O_2 to form a radical species ($O_2^{\bullet -}$) with simultaneous reoxidation of the dopant ion. The radical is able to efficiently undergo other photocatalytic processes leading to the degradation of the organic species. In the case of Ce-doped ZnO, the reoxidation step is known to be hindered because the potential is more positive that that of $O_2/O_2^{\bullet -}$. Therefore, the photocatalytic activity of Ce-doped ZnO is lower in comparison with that of undoped ZnO. An additional/alternative reason for the improved photocatalytic performance with rare-earth-doped ZnO is indicated by the change in the relative intensities of the (0002) and $(10\bar{1}0)$ XRD peaks (see Figure 3). It has been reported that an increase in the aspect ratio of ZnO particles, accompanied by the formation of nanorods, leads to significantly higher photocatalytic activity. The nanorods have relatively fewer recombination centers with a smaller number of interparticle junctions and increased electron delocalization, which means that electrons can flow in the longitudinal direction of the ZnO crystal.[65,66] Therefore, a larger number of photogenerated electrons and holes are available for degradation of the MB dye, leading to higher photocatalytic efficiencies. In the work presented here, it was shown that an increase in the $(0002)/(10\bar{1}0)$ XRD peak intensity ratio was a result of the nanorod morphology (cf. samples ZnO-a and ZnO-b in Figures 1 and 3), which is likely to hold for all of the rare-earth-doped ZnO samples. Sulfur doping increased the photocatalytic activity compared with the undoped level, whereas Ga^{3+} doping reduced the photocatalytic activity. Ga doping also reduced the activity for the decolorization of MB, which could be attributed to a reduction in the number of oxygen vacancies.

■ CONCLUSIONS

A library of doped zinc oxide crystalline nanopowders was synthesized in a single rapid step using a CHFS reactor. The library consisted of 54 doped samples (18 different dopant ions at three concentration levels plus two undoped samples). The structures and properties of these nanopowders were investigated to identify structure—property—composition relationships on the basis of the BET specific surface area, crystallite size, photocatalytic activity, color, and UV—visible absorption.

Transition metal dopants tended to reduce photocatalytic activity because they form levels deep in the band gap that acted as recombination centers. Fe-, Ag-, Mn-, V-, Ni-, and Cr-doped samples all had a pale color and significantly suppressed photocatalytic activity. In general, increasing the doping concentration caused further decreases in the photocatalytic activity, with 1.5 atom % doped sample being less active than the 0.5 atom % one. Silver and vanadium dopants were the exceptions to this, which may be explained by a change in oxidation state of vanadium and possibly by a change in location of the silver ions. Fe-, Ag-, Mn-, Ni-, and Cr-doped ZnO may be more suitable candidates for UV attenuation because of their small (<100 nm) size, low photocatalytic activity, and good UV absorption. Ideally, UV attenuators would have no visible absorption, but these samples had a faint color and may have acceptable optical properties once dispersed. Co- and Ti-doped zinc oxide had reasonable photocatalytic activity, comparable to that of P25 and may be acceptable for some photocatalytic applications. Tests with a range of substrates and photoelectrochemical testing as well as toxicity tests would provide a clearer picture of acceptable uses.

Rare earth ions in general increased the photocatalytic activity. The order of activity for the decolorization of MB was 1.0Nd > 1.0Pr > 0.5Y > 0.5Gd > 0.5La > 1.0Er > ZnO ≫ 1.0Ce (using most active catalyst for each dopant). In general, low dopant concentrations were more beneficial to activity, with 0.5 or 1.0 atom % doped samples having greater activity in all cases. This was due to the large size of the rare earth ions, which limits their substitution into the ZnO lattice; at high concentrations they are likely to act as defect sites, which promote recombination. The photodecolorization activities of the rare-earth-doped ZnO were higher than that of undoped zinc oxide by up to a factor of 2 and far exceeded that of the commercial photocatalyst P25. These materials may be promising candidates for photocatalytic applications. Ce doping suppressed the activity of ZnO, and Ce-doped ZnO may be a useful UV-attenuator material.

■ EXPERIMENTAL PROCEDURES

Zinc nitrate hexahydrate [$Zn(NO_3)_2{\cdot}6H_2O$, technical grade (>98%)], praseodymium nitrate hexahydrate [$Pr(NO_3)_3{\cdot}6H_2O$, >99.9%], neodymium nitrate hexahydrate [$Nd(NO_3)_3{\cdot}6H_2O$, >99.9%], gadolinium nitrate hexahydrate [$Gd(NO_3)_3{\cdot}6H_2O$, >99.9%], erbium nitrate hexahydrate [$Er(NO_3)_3{\cdot}6H_2O$, >99.9%], lanthanum nitrate hexahydrate [$La(NO_3)_3{\cdot}9H_2O$, >99%], yttrium nitrate hexahydrate [$Y(NO_3)_3{\cdot}6H_2O$, >99.9%], iron nitrate nonahydrate [$Fe(NO_3)_3{\cdot}9H_2O$, >98%], strontium nitrate [$Sr(NO_3)_2$, >99%], cobalt nitrate hexahydrate [$Co(NO_3)_2{\cdot}6H_2O$, >98%], gallium nitrate nonahydrate [$Ga(NO_3)_3{\cdot}9H_2O$, >99.9%], nickel nitrate hexahydrate [$Ni(NO_3)_2{\cdot}6H_2O$], manganese nitrate [$Mn(NO_3)_2{\cdot}4H_2O$, >96%], and chromium nitrate nonahydrate [$Cr(NO_3)_3{\cdot}9H_2O$, >99%] were used without modification as obtained from Sigma-Aldrich (Dorset, UK). MB (>96%), thiourea (NH_2CSNH_2, >99%), cerium ammonium nitrate [$Ce(NH_4)_2(NO_3)_6$, CAN, >98.5%), silver nitrate ($AgNO_3$, >99.9%), and vanadyl oxysulfate ($VOSO_4{\cdot}H_2O$, >99.9%) were obtained from Fisher (Loughborough, UK). Potassium hydroxide pellets (analytical grade) were obtained from Merck (Frankfurt, Germany). In all cases, deionized water (>10 MΩ) was used for the precursor solution, synthesis, and testing. Aeroxide P25 TiO_2 from Evonik was used as a reference material for comparisons of photocatalytic activity.

Undoped zinc oxide was made in the CHFS system (Figure 9), the basic design of which has been reported elsewhere.[23,67−69] For the synthesis of undoped zinc oxide, a room-temperature aqueous solution of 0.2 M zinc nitrate hexahydrate (pump P2) was pumped to meet an aqueous flow of room-temperature 0.2 M KOH (pump P3) at a T-piece (Figure 9). This mixed feed then met a feed of superheated water (450 °C and 24.1 MPa) in a mixer (R in Figure 9), whereupon the particles were produced in a continuous flow.[70] Herein, flow rates of 20, 10, and 10 mL min^{-1} were used for the superheated water feed, the mixed metal ion feed, and the base feed, respectively. The aqueous nanoparticle slurry was then cooled as it passed through a cold-water-jacketed pipe and then collected continuously from the exit of the backpressure regulator (Tescom model 26-1762-24). This high-throughput synthesis process is described in some detail elsewhere,[71,72] while more information on the scale-up to kilogram per hour quantities in a CHFS pilot-plant process, for the production of ZnO and its doped mixtures and other metal oxides, using a scalable confined jet mixer, can be found in recent publications by the authors.[73,74] The sample of unmodified nano-ZnO obtained using the current process is labeled as ZnO-a. A second sample of undoped ZnO was made by the same method except that 10% (v/v) H_2O_2 (3.3 M) was added to the 0.2 M zinc nitrate feed; this sample is identified as ZnO-b.

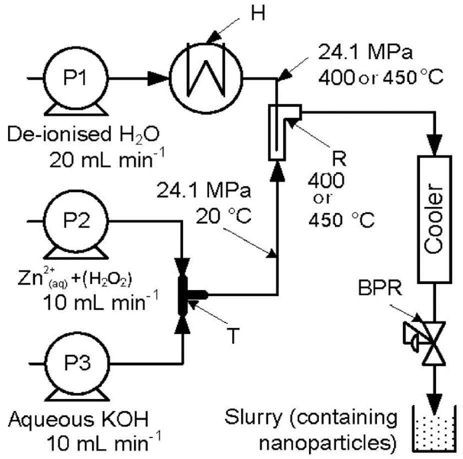

Figure 9. Schematic representation of the CHFS system for the synthesis of zinc oxide nanomaterials.

A series of 56 doped nano-ZnO samples were produced in the CHFS system (18 dopants at three different concentrations) with a mixed Zn^{2+} and dopant metal ion feed (pump P2). Each precursor solution was made by adding the appropriate dopant metal ion to zinc nitrate at a total metal ion concentration of 0.2 M. The concentrations of dopant ions were 0.5, 1.0, and 1.5 atom % (with respect to zinc). The samples are labeled according to the dopant ion and its concentration in the precursor solution feed. For example, the sample containing 1.5 atom % Er with respect to Zn is labeled as 1.5Er. For cleanup, each of the slurries was collected from the exit of the backpressure regulator, placed in a 50 mL centrifuge tube, and centrifuged at 5100 rpm for 20 min. The supernatant was then removed (ca. 40 mL) and replaced with 40 mL of clean deionized water, and the solid was redispersed using a vortex mixer (VWR model VM-3000) for 2 min and ultrasonicated for 5 min (30 W ultrasonic bath, VWR USC100T), after which each tube was further centrifuged at 5100 rpm for 30 min. This cleaning procedure was repeated twice with a final removal of 40 mL of liquid. The wet concentrated solids were freeze-dried for 22 h at 1.3 × 10^{-7} mBar (Virtis Genesis 35XL). The entire library was synthesized over three reactions on three days and consisted of 24 h of reaction time. Fresh samples of ZnO-a and ZnO-b were made at the start of each day. One additional sample each of ZnO-a and ZnO-b was synthesized at a later date to assess reproducibility. A photograph of the doped ZnO nanopowder library is shown in Figure 10.

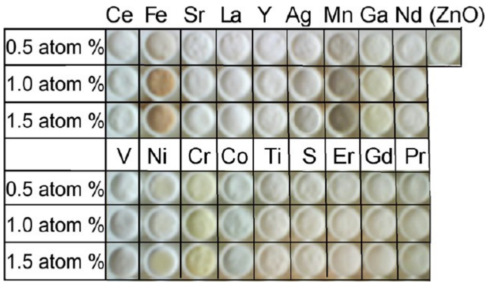

Figure 10. Photograph of the doped ZnO nanopowder library arranged by dopant and concentration.

XRD analyses were carried out on an X-pert Pro PW3064/60 diffractometer with a high-throughput stage to collect powder XRD data for the two pure ZnO samples and the doped ZnO samples. Continuous scans were collected over the 2θ = 5−120° range with a step size of 0.02° and a dwell time of 2 s per step (these data are shown in the Supporting Information). Repeated measurements on separate ZnO-a and -b samples revealed no significant differences. The particle sizes and morphologies of selected "as-prepared" nanopowders were investigated using a high-resolution transmission electron microscope (JEOL model 4000EX) at Oxford University (Oxford, UK) at an accelerating voltage of 400 kV. Samples were collected on carbon-coated copper grids (holey carbon film, 300 mesh Cu; Agar Scientific, Essex, UK) after being briefly dispersed ultrasonically (Kerry ultrasonic bath, Skipton, UK) in ethanol for 3 min. Particle size analysis was performed using Gatan Digital Micrograph particle size analysis software.

BET surface area measurements were performed on a six-station Micromeritics ASAP 2420 analyzer (N_2 adsorption). The powders were degassed at 200 °C in N_2 (BOC, UK) for 5 h prior to BET analyses, as ZnO is hydroscopic. These conditions were chosen as the degassing conditions after a time−temperature assay for as-prepared ZnO nanopowders to reach a level of no further weight loss due to adsorbed water. When degassing was not carried out under these conditions, the observed surface areas were lower because of insufficient removal of surface water. ZnO-a and ZnO-b from four separate reactions were tested to provide an evaluation of the error in the surface area measurements. In each case, the measurement was consistent to 1 $m^2\ g^{-1}$.

The optical properties, including the absorption and reflection spectra and the color, were measured using an Ocean Optics spectrophotometer (USB 4000) with a deuterium halogen light source (DH-2000-BAL), 400 μm fiber optic cables (QR400-7-UV-vis), and SpectraSuite software. UV−vis spectra were collected using a reflectance probe (QR400-7-UV-vis) with reference to a white reflectance standard with Spectralon (Ocean Optics WS-1-S). Additionally, the band gaps were calculated using the Kubelka−Munk (KM) function (eq 1) via conversion of the reflectance (R) spectra. For band-gap calculations, $[F_{KM}(R)\cdot h\nu]^2$ was plotted against the photon energy, and the band-gap energy was measured from the distinct linear regime that denoted the onset of absorption. The UV−vis spectra of all six ZnO-a and ZnO-b samples were consistent, and the calculated band gaps were within 0.01 eV.

$$F_{KM} = \frac{(1 - R^2)}{2R} \qquad (1)$$

XPS experiments on selected samples were performed with a Kratos Axis Ultra-DLD photoelectron spectrometer using monochromatic Al Kα radiation (photon energy = 1486.6 eV, power = 150 W). Survey scans were performed at a pass energy (PE) of 160 eV, while detailed scans were performed at a PE of 40 eV. All of the data were analyzed using CasaXPS software (version 2.3.14). Spectra were acquired using a Kratos immersion lens charge neutralization system, and all of the spectra were subsequently calibrated to the C 1s signal, which was assigned a value of 284.7 eV and was attributable to adventitious carbon. Curve fits were performed using a Shirley background and a Gaussian peak shape with 30% Lorentzian character.

A parallel photocatalytic reactor system similar to that described and tested elsewhere by the authors[51] was constructed. It consisted of nine 50 mL glass beakers (Duran; the light absorption in the range 310 nm ≤ λ ≤ 2200 nm was negligibly low; the transmission spectrum is shown in Figure S6 in the Supporting Information) arranged circularly. The light source was a fan-cooled 400 W high-pressure Hg discharge lamp (400HPLR, Philips, RS Components; the spectral output is shown in Figure S7 in the Supporting Information). A frosted glass screen (23 cm diameter, 0.4 cm thick; First Mirrors, Bow, London, UK) was used as a light diffuser to ensure even illumination. The UV irradiance under the glass screen was measured as ca. 2.7 mW cm^{-2} (J-221 UV Meter, Ultra Violet Products, Cambridge, UK). UV−vis absorption spectra of the MB solution were recorded using an Ocean Optics spectrophotometer (USB 4000) with a deuterium halogen light source (DH-2000-BAL) and 6 μm fiber optic cables. The absorption spectrum of as-prepared MB dye is shown in Figure S8 in the Supporting Information. The photocatalytic activity of the nanopowders was evaluated by measuring the photodecolorization of aqueous MB dye under illumination with access to air. For a photocatalytic test, 0.01 g of the relevant photocatalyst was suspended in 50 mL of standard MB solution (4.0 × 10^{-5} M) in each of nine reactors.[69] The mixtures were magnetically stirred for 30 min in the absence of light in order to allow the dye to reach an equilibrium adsorption on the catalyst surface. The samples were then irradiated with light, and at 15 min intervals the light was switched off and 5.0 mL aliquots were temporarily removed from each bulk suspension. These samples were briefly centrifuged (5 min at 5100 rpm), and then the remaining dye was analyzed via UV−vis spectrophotometry (Ocean Optics USB 400 with 600 μm UV/vis optimized fibers) by measuring the absorbance intensity at 664 nm. The quantitative determination of unreacted dye was calculated using a calibrated correlation between the measured absorbance and its concentration.

■ ASSOCIATED CONTENT

Ⓢ Supporting Information

Powder XRD data, analysis of the high-resolution XPS dopant envelopes, calculated band-gap data, color data, and UV−vis spectra. This material is available free of charge via the Internet at http://pubs.acs.org.

■ AUTHOR INFORMATION

Corresponding Author

*E-mail: j.a.darr@ucl.ac.uk.

Present Address

§J.G.: UK Catalysis Hub, Research Complex at Harwell, Rutherford Appleton Laboratory, Harwell Oxford, Oxon OX11 0FA, United Kingdom.

Author Contributions

The manuscript was written through contributions of all authors. All authors have given approval to the final version of the manuscript.

Funding

The EPSRC is thanked for funding the High Throughput Nanoceramics Discovery Project (J.A.D., EPSRC Grant Reference EP/D038499/1). Sun Chemical (J.G.) is also thanked for supporting the Industrial CASE Award.

Notes

The authors declare no competing financial interest.

■ ACKNOWLEDGMENTS

Professor D. Cockayne and Drs. L. Karlsson, J. Hutchinson, and C. Hetherington at Oxford Department of Materials are thanked for assistance and access to the HRTEM instrument (under the EPSRC Access Scheme, Grant Reference EP/F01919X/1). Ignacio Villar and Emily Smith from the University of Nottingham (EPSRC Grant EP/F019750/1) are thanked for assistance and access to the XPS instrument.

■ REFERENCES

(1) Ji, S. L.; Ye, C. H. Synthesis, growth mechanism, and applications of zinc oxide nanomaterials. *J. Mater. Sci. Technol.* **2008**, *24* (4), 457−472.

(2) Steudel, R.; Steudel, Y. Interaction of zinc oxide clusters with molecules related to the sulfur vulcanization of polyolefins ("rubber"). *Chem.—Eur. J.* **2006**, *12* (33), 8589−8602.

(3) Saracz, A.; Hoffmann, E. Evaluation of Paint for Fungus Resistance—Zinc Oxide Latex Paints. *J. Oil Colour Chem. Assoc.* **1968**, *51* (2), 103−107.

(4) Huang, Y. Q.; Liu, M. D.; Jiang, S. L.; Zeng, Y. K.; Li, C. R.; Liu, S. B.; Zhou, D. X. Preparation and electrical properties of ZnO-glass ceramic films. *Microelectron. Eng.* **2003**, *66* (1−4), 760−766.

(5) Liu, H. S.; Chin, T. S.; Yung, S. W. FTIR and XPS studies of low-melting PbO−ZnO−P_2O_5 glasses. *Mater. Chem. Phys.* **1997**, *50* (1), 1−10.

(6) Zhang, D. H. Adsorption and photodesorption of oxygen on the surface and crystallite interfaces of sputtered ZnO films. *Mater. Chem. Phys.* **1996**, *45* (3), 248−252.

(7) Water, W.; Chu, S. Y. Physical and structural properties of ZnO sputtered films. *Mater. Lett.* **2002**, *55* (1−2), 67−72.

(8) Music, S.; Dragcevia, D.; Popovic, S.; Ivanda, M. Precipitation of ZnO particles and their properties. *Mater. Lett.* **2005**, *59* (19−20), 2388−2393.

(9) Wang, C.; Wang, E.; Shen, E.; Gao, L.; Kang, Z.; Tian, C.; Zhang, C.; Lan, Y. Growth of ZnO nanoparticles from nanowhisker precursor with a simple solvothermal route. *Mater. Res. Bull.* **2006**, *41* (12), 2298−2302.

(10) Perkins, C. L.; Lee, S. H.; Li, X. N.; Asher, S. E.; Coutts, T. J. Identification of nitrogen chemical states in N-doped ZnO via X-ray photoelectron spectroscopy. *J. Appl. Phys.* **2005**, *97* (3), No. 034907.

(11) Hsiao, K. C.; Liao, S. C.; Chen, Y. J. Synthesis, characterization and photocatalytic property of nanostructured Al-doped ZnO powders prepared by spray pyrolysis. *Mater. Sci. Eng., A* **2007**, *447* (1−2), 71−76.

(12) Rajalakshmi, M.; Arora, A. K.; Bendre, B. S.; Mahamuni, S. Optical phonon confinement in zinc oxide nanoparticles. *J. Appl. Phys.* **2000**, *87* (5), 2445−2448.

(13) Shan, F. K.; Liu, G. X.; Lee, W. J.; Shin, B. C. Hexagonal zinc oxide thin films on cubic MgO (100) substrates deposited by pulsed laser deposition. *Integr. Ferroelectr.* **2006**, *78*, 181−190.

(14) Cao, H. T.; Pei, Z. L.; Gong, J.; Sun, C.; Huang, R. F.; Wen, L. S. Preparation and characterization of Al and Mn doped ZnO (ZnO:(Al,Mn)) transparent conducting oxide films. *J. Solid State Chem.* **2004**, *177* (4−5), 1480−1487.

(15) Fan, Z. Y.; Lu, J. G. Zinc oxide nanostructures: Synthesis and properties. *J. Nanosci. Nanotechnol.* **2005**, *5* (10), 1561−1573.

(16) Wang, Z. L. Zinc oxide nanostructures: Growth, properties and applications. *J. Phys.: Condens. Matter* **2004**, *16* (25), R829−R858.

(17) Sue, K.; Murata, K.; Kimura, K.; Arai, K. Continuous synthesis of zinc oxide nanoparticles in supercritical water. *Green Chem.* **2003**, *5* (5), 659−662.

(18) Sue, K.; Kimura, K.; Arai, K. Hydrothermal synthesis of ZnO nanocrystals using microreactor. *Mater. Lett.* **2004**, *58* (25), 3229−3231.

(19) Sue, K.; Kimura, K.; Murata, K.; Arai, K. Effect of cations and anions on properties of zinc oxide particles synthesized in supercritical water. *J. Supercrit. Fluids* **2004**, *30* (3), 325−331.

(20) Sue, K.; Kimura, K.; Murata, K.; Arai, K. Hydrothermal synthesis of zinc oxide crystals in homogeneous mixture of carbon dioxide, hydrogen, and water. *Chem. Lett.* **2004**, *33* (6), 708−709.

(21) Viswanathan, R.; Gupta, R. B. Formation of zinc oxide nanoparticles in supercritical water. *J. Supercrit. Fluids* **2003**, *27* (2), 187−193.

(22) Viswanathan, R.; Lilly, G. D.; Gale, W. F.; Gupta, R. B. Formation of zinc oxide−titanium dioxide composite nanoparticles in supercritical water. *Ind. Eng. Chem. Res.* **2003**, *42* (22), 5535−5540.

(23) Kellici, S.; Gong, K.; Lin, T.; Brown, S.; Clark, R. J. H.; Vickers, M.; Cockcroft, J. K.; Middelkoop, V.; Barnes, P.; Perkins, J. M.; Tighe, C. J.; Darr, J. A. High-throughput continuous hydrothermal flow synthesis of Zn−Ce oxides: Unprecedented solubility of Zn in the nanoparticle fluorite lattice. *Philos. Trans. R. Soc. London, Ser. A* **2010**, *368* (1927), 4331−4349.

(24) Choi, W. Y.; Termin, A.; Hoffmann, M. R. The Role of Metal-Ion Dopants in Quantum-Sized TiO_2—Correlation between Photoreactivity and Charge-Carrier Recombination Dynamics. *J. Phys. Chem.* **1994**, *98* (51), 13669−13679.

(25) Xu, A. W.; Gao, Y.; Liu, H. Q. The preparation, characterization, and their photocatalytic activities of rare-earth-doped TiO_2 nanoparticles. *J. Catal.* **2002**, *207* (2), 151−157.

(26) Zhu, J. F.; Chen, F.; Zhang, J. L.; Chen, H. J.; Anpo, M. Fe^{3+}−TiO_2 photocatalysts prepared by combining sol−gel method with hydrothermal treatment and their characterization. *J. Photochem. Photobiol., A* **2006**, *180* (1−2), 196−204.

(27) Anandan, S.; Vinu, A.; Lovely, K.; Gokulakrishnan, N.; Srinivasu, P.; Mori, T.; Murugesan, V.; Sivamurugan, V.; Ariga, K. Photocatalytic activity of La-doped ZnO for the degradation of monocrotophos in aqueous suspension. *J. Mol. Catal. A: Chem.* **2007**, *266* (1−2), 149−157.

(28) Wang, R. H.; Xin, J. H. Z.; Yang, Y.; Liu, H. F.; Xu, L. M.; Hu, J. H. The characteristics and photocatalytic activities of silver doped ZnO nanocrystallites. *Appl. Surf. Sci.* **2004**, *227* (1−4), 312−317.

(29) Qiu, X. Q.; Li, G. S.; Sun, X. F.; Li, L. P.; Fu, X. Z. Doping effects of Co^{2+} ions on ZnO nanorods and their photocatalytic properties. *Nanotechnology* **2008**, *19* (21), No. 215703.

(30) Dodd, A.; McKinley, A.; Tsuzuki, T.; Saunders, M. Tailoring the photocatalytic activity of nanoparticulate zinc oxide by transition metal oxide doping. *Mater. Chem. Phys.* **2009**, *114* (1), 382−386.

(31) Fichou, D.; Pouliquen, J.; Kossanyi, J.; Jakani, M.; Campet, G.; Claverie, J. Extension of the Photoresponse of Semiconducting Zinc-Oxide Electrodes by 3D-Impurities Absorbing in the Visible Region of the Solar Spectrum. *J. Electroanal. Chem.* **1985**, *188* (1−2), 167−187.

(32) Jakani, M.; Campet, G.; Claverie, J.; Fichou, D.; Pouliquen, J.; Kossanyi, J. Photoelectrochemical Properties of Zinc-Oxide Doped with 3D Elements. *J. Solid State Chem.* **1985**, *56* (3), 269−277.

(33) Deng, Y.; Wang, G. S.; Li, N.; Guo, L. Synthesis and red-shifted photoluminescence of single-crystalline ZnO nanowires. *J. Lumin.* **2009**, *129* (1), 55−58.

(34) Demianets, L. N.; Kostomarov, D. V. Mechanism of zinc oxide single crystal growth under hydrothermal conditions. *Ann. Chim.* **2001**, *26* (1), 193−198.

(35) Li, W. J.; Shi, E. W.; Zhong, W. Z.; Yin, Z. W. Growth mechanism and growth habit of oxide crystals. *J. Cryst. Growth* **1999**, *203* (1−2), 186−196.

(36) Li, D.; Haneda, H.; Ohashi, N.; Saito, N.; Hishita, S. Morphological reform of ZnO particles induced by coupling with MO_x (M = V, W, Ce) and the effects on photocatalytic activity. *Thin Solid Films* **2005**, *486* (1−2), 20−23.

(37) Pandey, B.; Ghosh, S.; Srivastava, R.; Kabiraj, D.; Shripati, T.; Lalla, N. R. Synthesis of nanodimensional ZnO and Ni-doped ZnO thin films by atom beam sputtering and study of their physical properties. *Physica E* **2009**, *41* (7), 1164−1168.

(38) Tay, Y.; Tan, T.; Liang, M.; Boey, F.; Li, S. Specific defects, surface band bending and characteristic green emissions of ZnO. *Phys. Chem. Chem. Phys.* **2010**, *12* (23), 6008−6013.

(39) Ariosa, D.; Elhordoy, F.; Dalchiele, E.; Marotti, R.; Stari, C. Texture vs morphology in ZnO nano-rods: On the X-ray diffraction characterization of electrochemically grown samples. *J. Appl. Phys.* **2011**, *110* (12), No. 124901.

(40) Chen, H. H.; Du Pasquier, A.; Saraf, G.; Zhong, J.; Lu, Y. Dye-sensitized solar cells using ZnO nanotips and Ga-doped ZnO films. *Semicond. Sci. Technol.* **2008**, *23* (4), No. 045004.

(41) Tao, Z. W.; Yu, X. B.; Liu, J.; Yang, L. Z.; Yang, S. P. A facile synthesis and photoluminescence of porous S-doped ZnO architectures. *J. Alloys Compd.* **2008**, *459* (1−2), 395−398.

(42) Demir, M. M.; Koynov, K.; Akbey, U.; Bubeck, C.; Park, I.; Lieberwirth, I.; Wegner, G. Optical properties of composites of PMMA and surface-modified zincite nanoparticles. *Macromolecules* **2007**, *40* (4), 1089−1100.

(43) Zhang, X. H.; Yan, X. Q.; Zhao, J.; Qin, Z.; Zhang, Y. Structure and photoluminescence of S-doped ZnO nanorod arrays. *Mater. Lett.* **2009**, *63* (3−4), 444−446.

(44) Singh, S.; Rao, M. S. R. Optical and electrical resistivity studies of isovalent and aliovalent 3d transition metal ion doped ZnO. *Phys. Rev. B* **2009**, *80* (4), No. 045210.

(45) Jing, L. Q.; Wang, B. Q.; Xin, B. F.; Li, S. D.; Shi, K. Y.; Cai, W. M.; Fu, H. G. Investigations on the surface modification of ZnO nanoparticle photocatalyst by depositing Pd. *J. Solid State Chem.* **2004**, *177* (11), 4221−4227.

(46) Jing, L. Q.; Xu, Z. L.; Sun, X. J.; Shang, J.; Cai, W. M. The surface properties and photocatalytic activities of ZnO ultrafine particles. *Appl. Surf. Sci.* **2001**, *180* (3−4), 308−314.

(47) Chen, M.; Wang, X.; Yu, Y. H.; Pei, Z. L.; Bai, X. D.; Sun, C.; Huang, R. F.; Wen, L. S. X-ray photoelectron spectroscopy and Auger electron spectroscopy studies of Al-doped ZnO films. *Appl. Surf. Sci.* **2000**, *158* (1−2), 134−140.

(48) Saeki, H.; Tabata, H.; Kawai, T. Magnetic and electric properties of vanadium doped ZnO films. *Solid State Commun.* **2001**, *120* (11), 439−443.

(49) Ajmal, A.; Majeed, I.; Malik, R. N.; Idriss, H.; Nadeem, M. A. Principles and mechanisms of photocatalytic dye degradation on TiO_2 based photocatalysts: A comparative overview. *RSC Adv.* **2014**, *4* (70), 37003−37026.

(50) Lam, S. M.; Sin, J. C.; Abdullah, A. Z.; Mohamed, A. R. Degradation of wastewaters containing organic dyes photocatalysed by zinc oxide: A review. *Desalin. Water Treat.* **2012**, *41* (1−3), 131−169.

(51) Thompson, K.; Goodall, J.; Kellici, S.; Mattinson, J. A.; Egerton, T. A.; Rehman, I.; Darr, J. A. Screening tests for the evaluation of nanoparticle titania photocatalysts. *J. Chem. Technol. Biotechnol.* **2009**, *84* (11), 1717−1725.

(52) Casey, P. S.; Rossouw, C. J.; Boskovic, S.; Lawrence, K. A.; Turney, T. W. Incorporation of dopants into the lattice of ZnO nanoparticles to control photoactivity. *Superlattices Microstruct.* **2006**, *39* (1−4), 97−106.

(53) Ullah, R.; Dutta, J. Photocatalytic degradation of organic dyes with manganese-doped ZnO nanoparticles. *J. Hazard. Mater.* **2008**, *156* (1−3), 194−200.

(54) Jaramillo, T. F.; Baeck, S. H.; Kleiman-Shwarsctein, A.; Choi, K. S.; Stucky, G. D.; McFarland, E. W. Automated electrochemical synthesis and photoelectrochemical characterization of $Zn_{1-x}Co_xO$ thin films for solar hydrogen production. *J. Comb. Chem.* **2005**, *7* (2), 264−271.

(55) Li, L. Y.; Wang, W. H.; Liu, H.; Liu, X. D.; Song, Q. G.; Ren, S. W. First Principles Calculations of Electronic Band Structure and Optical Properties of Cr-Doped ZnO. *J. Phys. Chem. C* **2009**, *113* (19), 8460−8464.

(56) Iketani, K.; Sun, R. D.; Toki, M.; Hirota, K.; Yamaguchi, O. Sol-gel-derived $V_xTi_{1-x}O_2$ films and their photocatalytic activities under visible light irradiation. *Mater. Sci. Eng., B* **2004**, *108* (3), 187−193.

(57) Qiu, X. Q.; Li, L. P.; Zheng, J.; Liu, J. J.; Sun, X. F.; Li, G. S. Origin of the enhanced photocatalytic activities of semiconductors: A case study of ZnO doped with Mg^{2+}. *J. Phys. Chem. C* **2008**, *112* (32), 12242−12248.

(58) Que, W.; Zhou, Y.; Lam, Y. L.; Pita, K.; Chan, Y. C.; Kam, C. H. Luminescence properties from erbium oxide nanocrystals dispersed in titania/organically modified silane composite sol−gel thin films. *Appl. Phys. A: Mater. Sci. Process.* **2001**, *73* (2), 209−213.

(59) Yan, B.; Zhou, K. In situ sol−gel composition of inorganic/organic polymeric hybrid precursors to synthesize red-luminescent $CaTiO_3:Pr^{3+}$ and $CaTi_{0.5}Zr_{0.5}O_3:Pr^{3+}$ phosphors. *J. Alloys Compd.* **2005**, *398* (1−2), 165−169.

(60) Liang, C. H.; Li, F. B.; Liu, C. S.; Lu, H. L.; Wang, X. G. The enhancement of adsorption and photocatalytic activity of rare earth ions doped TiO_2 for the degradation of Orange I. *Dyes Pigm.* **2008**, *76* (2), 477−484.

(61) Anandan, S.; Vinu, A.; Mori, T.; Gokulakrishnan, N.; Srinivasu, P.; Murugesan, V.; Ariga, K. Photocatalytic degradation of 2,4,6-trichlorophenol using lanthanum doped ZnO in aqueous suspension. *Catal. Commun.* **2007**, *8* (9), 1377−1382.

(62) Mishra, B. G.; Rao, G. R. Promoting effect of ceria on the physicochemical. and catalytic properties of CeO_2−ZnO composite oxide catalysts. *J. Mol. Catal. A: Chem.* **2006**, *243* (2), 204−213.

(63) de Lima, J. F.; Martins, R. F.; Neri, C. R.; Serra, O. A. ZnO:CeO_2-based nanopowders with low catalytic activity as UV absorbers. *Appl. Surf. Sci.* **2009**, *255* (22), 9006−9009.

(64) Sin, J. C.; Lam, S. M.; Lee, K. T.; Mohamed, A. R. Preparation of rare earth-doped ZnO hierarchical micro/nanospheres and their enhanced photocatalytic activity under visible light irradiation. *Ceram. Int.* **2014**, *40* (4), 5431−5440.

(65) Zhang, X. Y.; Qin, J. Q.; Xue, Y. N.; Yu, P. F.; Zhang, B.; Wang, L. M.; Liu, R. P. Effect of aspect ratio and surface defects on the photocatalytic activity of ZnO nanorods. *Sci. Rep.* **2014**, *4*, No. 4596.

(66) Leelavathi, A.; Madras, G.; Ravishankar, N. Origin of enhanced photocatalytic activity and photoconduction in high aspect ratio ZnO nanorods. *Phys. Chem. Chem. Phys.* **2013**, *15* (26), 10795−10802.

(67) Boldrin, P.; Hebb, A. K.; Chaudhry, A. A.; Otley, L.; Thiebaut, B.; Bishop, P.; Darr, J. A. Direct synthesis of nanosized $NiCo_2O_4$ spinel and related compounds via continuous hydrothermal synthesis methods. *Ind. Eng. Chem. Res.* **2007**, *46* (14), 4830−4838.

(68) Zhang, Z.; Brown, S.; Goodall, J. B. M.; Weng, X.; Thompson, K.; Gong, K.; Kellici, S.; Clark, R. J. H.; Evans, J. R. G.; Darr, J. A. Direct continuous hydrothermal synthesis of high surface area nanosized titania. *J. Alloys Compd.* **2009**, *476* (1−2), 451−456.

(69) Weng, X. L.; Boldrin, P.; Abrahams, I.; Skinner, S. J.; Kellici, S.; Darr, J. A. Direct syntheses of $La_{n+1}Ni_nO_{3n+1}$ phases (n = 1, 2, 3 and infinity) from nanosized co-crystallites. *J. Solid State Chem.* **2008**, *181* (5), 1123−1132.

(70) Gruar, R.; Tighe, C. J.; Reilly, L. M.; Sankar, G.; Darr, J. A. Tunable and rapid crystallisation of phase pure Bi_2MoO_6 (koechlinite) and $Bi_2Mo_3O_{12}$ via continuous hydrothermal synthesis. *Solid State Sci.* **2010**, *12* (9), 1683−1686.

(71) Weng, X. L.; Cockcroft, J. K.; Hyett, G.; Vickers, M.; Boldrin, P.; Tang, C. C.; Thompson, S. P.; Parker, J. E.; Knowles, J. C.; Rehman, I.; Parkin, I.; Evans, J. R. G.; Darr, J. A. High-Throughput Continuous Hydrothermal Synthesis of an Entire Nanoceramic Phase Diagram. *J. Comb. Chem.* **2009**, *11* (5), 829−834.

(72) Quesada-Cabrera, R.; Weng, X. L.; Hyet, G.; Clark, R. J. H.; Wang, X. Z.; Darr, J. A. High-Throughput Continuous Hydrothermal Synthesis of Nanomaterials (Part II): Unveiling the As-Prepared $Ce_xZr_yY_zO_{2-\delta}$ Phase Diagram. *ACS Comb. Sci.* **2013**, *15* (9), 458−463.

(73) Tighe, C. J.; Cabrera, R. Q.; Gruar, R. I.; Darr, J. A. Scale Up Production of Nanoparticles: Continuous Supercritical Water Synthesis of Ce−Zn Oxides. *Ind. Eng. Chem. Res.* **2013**, *52* (16), 5522−5528.

(74) Gruar, R. I.; Tighe, C. J.; Darr, J. A. Scaling-Up a Confined Jet Reactor for the Continuous Hydrothermal Manufacture of Nanomaterials. *Ind. Eng. Chem. Res.* **2013**, *52* (15), 5270−5281.